

CarNet: A Lightweight and Efficient Encoder-Decoder Architecture for High-quality Road Crack Detection

Kai Li, Yingjie Tian, and Zhiqian Qi

Abstract—Pixel-wise crack detection is a challenging task because of poor continuity and low contrast in cracks. The existing frameworks usually employ complex models leading to good accuracy and yet low inference efficiency. In this paper, we present a lightweight encoder-decoder architecture, CarNet, for efficient and high-quality crack detection. To this end, we first propose that the ideal encoder should present an olive-type distribution about the number of convolutional layers at different stages. Specifically, as the network stages deepen in the encoder, the number of convolutional layers shows a downward trend after the model input is compressed in the initial network stage. Meanwhile, in the decoder, we introduce a lightweight up-sampling feature pyramid module to learn rich hierarchical features for crack detection. In particular, we compress the feature maps of the last three network stages to the same channels and then employ up-sampling with different multiples to resize them to the same resolutions for information fusion. Finally, extensive experiments on four public databases, i.e., Sun520, Rain365, BJJN260, and Crack360, demonstrate that our CarNet gains a good trade-off between inference efficiency and test accuracy over the existing state-of-the-art methods.

Index Terms—Crack detection, light-weight, efficient inference, encoder-decoder.

I. INTRODUCTION

CRACKS, as common defects, are the sign of road damage. Even weak pavement cracks may easily form potholes of different sizes after being washed on a rainy night, which will bring potential dangers to high-speed vehicles. Timely detecting and repairing cracks could prevent damage expansion and ensure traffic safety, and also reduce the high cost of repairing deteriorated cracks. Thus, automatic methods for crack detection are greatly desired to improve efficiency and reduce the cost.

Up to date, it is greatly challenging to exploit a fully automatic algorithm for pixel-wise crack detection in practice. Generally, numerous cracks exhibit poor continuity and low contrast, which are caused by many interference factors, including shadows on sunny days, rainwater on rainy days, uneven illuminations in night scenes, and grain-like texture in the background, as shown in Fig. 1.

This work has been partially supported by grants from National Natural Science Foundation of China (Nos. 12071458, and 71731009).

Kai Li is with the School of Mathematics Sciences, University of Chinese Academy of Sciences, Beijing 100049, China.(e-mail: likai14@mails.ucas.ac.cn)

Yingjie Tian and Zhiqian Qi are with the Research Center on Fictitious Economy and Data Science, Chinese Academy of Sciences, Beijing 100190, China; with the Key Laboratory of Big Data Mining and Knowledge Management, Chinese Academy of Sciences, Beijing 100190, China.

Corresponding Authors: Yingjie Tian (e-mail: tyj@ucas.ac.cn)

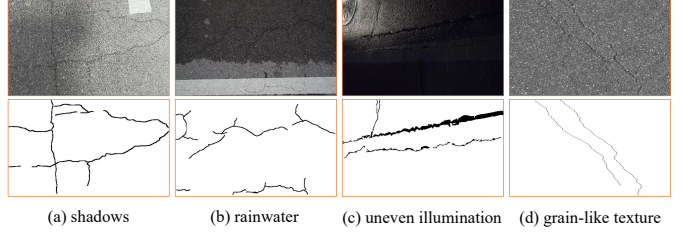


Fig. 1. Visual examples of different interference factors. (a), (b), (c), and (d) contain shadows on sunny days, rainwater on rainy days, uneven illuminations in night scenes, and grain-like texture in the background, respectively. The above images and their ground-truth originate from four road crack databases, i.e., our Sun520, our Rain365, BJJN260 [1], and Crack360 [2], respectively.

Recently, based on automatic feature extraction, deep convolutional neural networks have shown striking improvement on methods depending on hand-crafted features in many computer vision tasks, such as image classification [3]–[5], object detection [6]–[9], edge detection [10]–[13], and image segmentation [14]–[16]. However, few models are developed for pixel-wise crack detection.

Luckily, if regarding cracks as linear or curvilinear objects, one can directly apply general edge detection and image segmentation systems for pixel-wise crack detection. These methods usually employ an encoder-decoder architecture, accompanied by one or more skip layers to fuse hierarchical convolutional features. For example, Xie et al. [10] develop a holistically-nested edge detection (HED) algorithm by utilizing a trimmed VGG16 [4] as the encoder and then applying five deeply-supervised branch networks and their fused branch network to construct the decoder. Chen et al. [16] propose a novel segmentation model DeepLabv3+ by using a modified ResNet101 [5] as its encoder and then utilizing a skip-layer to fuse high- and low-level features in its decoder. For crack detection, despite obtaining good accuracy, these methods are embarrassing in terms of detection efficiency. Because of using multi-classification models for ImageNet [17] as the encoders, they tough upon too many redundant parameters and calculations, and thereby hardly implement efficient inference.

Meanwhile, image segmentation methods for street scenes are increasingly emerging with the recent development of autonomous driving. Compared with the above general image segmentation models, the image segmentation systems for street scenes pay more attention to inference efficiency, which seems to bring new dawns for efficient crack detection. The existing efficient segmentation approaches for images in street

scenes, such as ENet [18] and ERFNet [19], usually apply early down-sampling strategies to compress model input to improve their efficiency. Meanwhile, these methods usually directly resize the output of encoders to the original input resolutions to construct their decoders. Although this manner helps improve inference efficiency, it sacrifices low-level features and spatial details, thereby easily missing some trivial cracks and then leading to a dramatic accuracy decrease.

In this paper, based on the advantages of the above two methods, we present a lightweight encoder-decoder architecture for efficient and high-quality road crack detection. First, to reduce model complexity and improve inference efficiency, we consider the ideal encoder about the number of the convolutional layers in different network stages. Specifically, in the initial stage, we employ the early down-sampling strategy introduced by ENet [18] to compress model input. Next, we propose that as network stages deepen, the number of the convolutional layers should show a downward trend in turn. Then, the structure of an ideal encoder is large in the middle and small in the two ends. For convenience, we named it the olive-type distribution.

Besides, motivated by HED [10] and Deeplab V3+ [16], we propose a novel decoder that combines hierarchical convolutional features while taking into account model complexity and inference efficiency. First, we develop a lightweight up-sampling feature pyramid block (UFPB) by using three 1×1 convolutions to compress feature maps at the last three network stages respectively and then conducting up-sampling with different multiples to fuse three-branch feature information. Next, to reduce model complexity and improve inference efficiency during restoring feature maps, we utilize two decomposition convolutions to supersede one convolution with a square kernel, and employ one 1×1 convolution and one deconvolution to replace one single deconvolution.

As the overall encoder-decoder network looks like a small car, we nominate it CarNet. To sum up, our contributions lie in four-fold:

- We construct two new pavement crack databases, Sun520 and Rain365. To our knowledge, in the open-source road crack datasets using pixel-level annotation, Sun520 is currently the largest one while Rain365 is the first one under the rain scene.
- We propose an olive-type encoder about the number of convolutional layers in different network stages to reduce model complexity and improve inference efficiency.
- We introduce a lightweight module UFPB in the decoder to get rich hierarchical features for pixel-wise crack detection.
- Extensive experiments on four public databases show that our CarNet yields better test accuracy than the existing state-of-the-art systems while achieving a comparable inference speed with the fastest two systems.

The rest is organized as follows. Section II briefly reviews the related work. Section III presents our architecture for pixel-wise crack detection. Section IV demonstrate experimentally the effectiveness of our methods. Finally, Section V gives a summary of our work. Besides, appendix A shows the performance of our method on edge detection tasks.

II. RELATED WORK

In this section, we start with pixel-wise crack detection systems based on shallow models, and next state some methods based on deep learning.

A. Shallow Models for Crack Detection

The traditional methods, such as wavelet transform [20], contrast ratio [21], texture-analysis [22], and minimal path selection [23]–[25], are on the basis of strict assumptions, such as the consistently darker characterized in brightness for real crack pixel contrasting to its neighbors. However, these approaches merely take into consideration the features of a single-pixel or the local neighboring correlation between pixels, which limit the ultimate performance of crack detection.

To address the above problem, traditional machine learning systems, such as [26]–[29], usually construct complex feature engineering by designing fussy handcrafted features, to reserve holistic structural information in images. For example, [27] redefines crack tokens by manually designed integral channel features, then presents a new descriptor to characterize road cracks, and next utilizes random structured forests (RSF) for crack detection. However, these methods are vulnerable to noise in the background, because they are still based on shallow models and then only obtain low-level features.

B. Deep Learning-Based for Crack Detection

In the following, we introduce some deep convolutional neural networks related to crack detection. According to whether the encoder and decoder are symmetrical or not, these methods can be roughly divided into two categories:

Symmetrical encoder-decoder networks. They usually utilize skip layers to merge the same scale feature maps from the encoder and the decoder respectively, to compensate for the loss of spatial information in the down-sampling process.

For instance, U-Net [30] takes full use of various skip-layer to combine information from the contracting path and the symmetric expanding path used to capture context and get precise localization respectively. U-CliqueNet [31] separates cracks from background by integrating alternately updated cliques [32] into U-Net.

The above two models employ channel concatenation to fuse the same scale feature maps. Different from them, SegNet [15] transfers the max-pooling indices in the feature maps of the encoder to the same resolution feature maps in the decoder. DeepCrack [2] gains hierarchical convolutional features for crack detection by taking advantage of up-sampling in SegNet and side-output in HED [10].

However, the symmetrical structure of the encoder and decoder often leads to excessive redundant parameters and calculations, and thus needs long-running time for inference. Besides, too many skip-layer connections reduce model parallelism and thus cut down inference efficiency.

Asymmetric encoder-decoder architectures. These models often apply one complex encoder to extract convolutional features, and then utilize one or more simple decoders to recover to the input resolution.

For example, some advanced systems based on edge detection, such as HED [10], RCF [11], BDCN [12], and BDP-Net [13], apply a trimmed VGG16 [4] as the encoder to extract features, and then use multiple up-sampling to directly resize the feature maps of different stages to the original input size to form the decoders. Recent image segmentation-based approaches, such as Deeplab V3+ [16] and CrackSeg [33], employ a modified ResNet50 or ResNet101 [5] as the encoder, and then utilize twice quadruple up-sampling to gradually recover the spatial information to construct the decoders. Besides, a two- or multi-branch structure is used to fuse hierarchical convolutional features in these models.

Note that these methods directly adopt multi-classification models for ImageNet [17] as their encoders, which brings heavy computation complexity and memory footprint. Besides, excessive branch structures are not friendly to the memory access cost, thereby cutting down inference efficiency further. Therefore, it is difficult for most models to conduct efficient inference in the end.

Meanwhile, the image segmentation systems for street scenes provide new ideas for efficient crack detection. For example, ENet [18] proposes that visual information is highly spatially redundant, and thus the input needs to be compressed by the proposed early down-sampling strategy. Apart from early down-sampling, ERFNet [19] introduces a novel non-bottleneck module by combining a residual connection and factorized convolutions, to reduce parameters and calculations. BiSeNet V1 [34] and BiSeNet V2 [35] present bilateral segmentation networks where the spatial path and the context path are designed to preserve spatial details and semantic information respectively. To build a real-time segmentation architecture, FastSCNN [36] incorporates a shared shallow network before spatial and context paths. However, in practice, due to the loss of spatial details in images, these models need to be further developed in terms of test accuracy.

To gain a good trade-off between inference efficiency and test accuracy, we introduce a novel asymmetric encoder-decoder architecture. Our method fully draws on the encoder advantage of the image segmentation methods for street scenes (i.e., using early down-sampling to speed up model efficiency) and the decoder superiority of the general edge detection and image segmentation systems (i.e., applying branch structure to fuse hierarchical features at different network stages). Below, we elaborate on them.

III. METHODOLOGY

In this section, we present the overall architecture of CarNet by our proposed encoder and decoder, respectively.

A. The Proposed Olive-type Encoder

In deep learning, ResNet [5] plays an important role in preventing the gradient explosion and disappearance. Because of being originally built for ImageNet [17], a large-scale visual recognition database, ResNet involves high model complexity. Thus, if we directly utilize ResNet as the encoder of crack detection models, the inference efficiency will be not so friendly as to affect its application in practice.

Generally, model complexity includes space complexity and time complexity. Space complexity can be roughly estimated by model parameters. Time complexity can be reflected by floating-point operations (FLOPs). Convolution operations are often used in neural networks. Taking a convolution operation with a bias term as an example, the corresponding parameters and FLOPs are respectively as follow:

$$\text{param} = (K_w * K_h * C_{in}) * C_{out} + C_{out}, \quad (1)$$

$$\text{FLOPs} = [(K_w * K_h * C_{in}) * C_{out} + C_{out}] * W_{out} * H_{out}. \quad (2)$$

Here, K_w and K_h represent the width and height of the convolutional kernel respectively. They are often set to 3 after the VGG series [4] come out. Besides, C_{in} and C_{out} indicate input and output channels respectively, W_{out} and H_{out} refer to width and height of the output feature map respectively.

As the network stages deepen, the convolutional channels will increase, and the resolution of feature maps will decrease. According to formula (1), to reduce model spatial complexity, the deeper network stages in the encoder should contain fewer convolutional layers. On the other hand, according to (2), *to cut down model time complexity, the ideal encoder should present an olive-type distribution about the number of convolutional layers in different network stages*. In other words, there should be more convolutional layers in the middle network stages, and fewer convolutional layers in the initial and tail stages. Such an idea mainly takes into account high resolution in the initial stage and large convolutional channels in the tail phase. In summary, we propose that *the number of convolutional layers decreases from the second network stage*.

Specifically, regarding the encoder, we propose the following design process:

First, we define the number of network stages. There are usually five stages in classification models, such as ResNet. To reduce space and time complexity in our encoder, we employ four stages corresponding to four down-sampling.

Second, we determine the number of convolutional layers in the initial stage. To speed up inference efficiency, we adopt the early down-sampling strategy introduced by ENet [18]. This strategy is conducted by the down-sampling block (DB).

As shown in Fig. 3 (a), in the DB module, the input is firstly fed to one 3×3 convolution and maximum pooling with stride 2 in a parallel way, respectively. Next, the feature maps from two-branch are fused by channel concatenation, and then further processed by batch normalization [37] and ReLU [38].

Third, we ascertain the number of the convolutional layers in the network tail and intermediate stages. Based on the olive-type distribution of encoders, the number of convolutional layers in the tail stage does not exceed a certain value.

For example, when using ResNet34 [5] as the benchmark, we can use two residual blocks in the tail network stage of our encoder, which correspond to four convolutional layers. Note that there are three residual modules in the tail stage of ResNet34. The residual block (RB), as shown in Fig. 3 (b), utilizes identity mapping as one skip-layer to fuse the input and the output of two stacked convolutional layers by an addition operation.

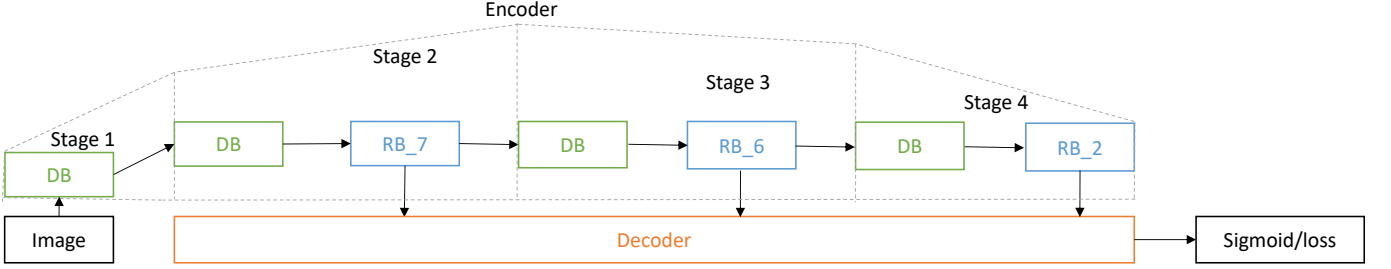


Fig. 2. The overall framework of our CarNet. Here, DB and RB refer to the down-sampling block and the residual block, respectively. RB_7 means that RB is used 7 times in a cascaded form. Decoder corresponds to our decoder network. Besides, in our encoder, the number of output channels after applying the DB module is 16, 64, 128, and 256 respectively unless otherwise specified.

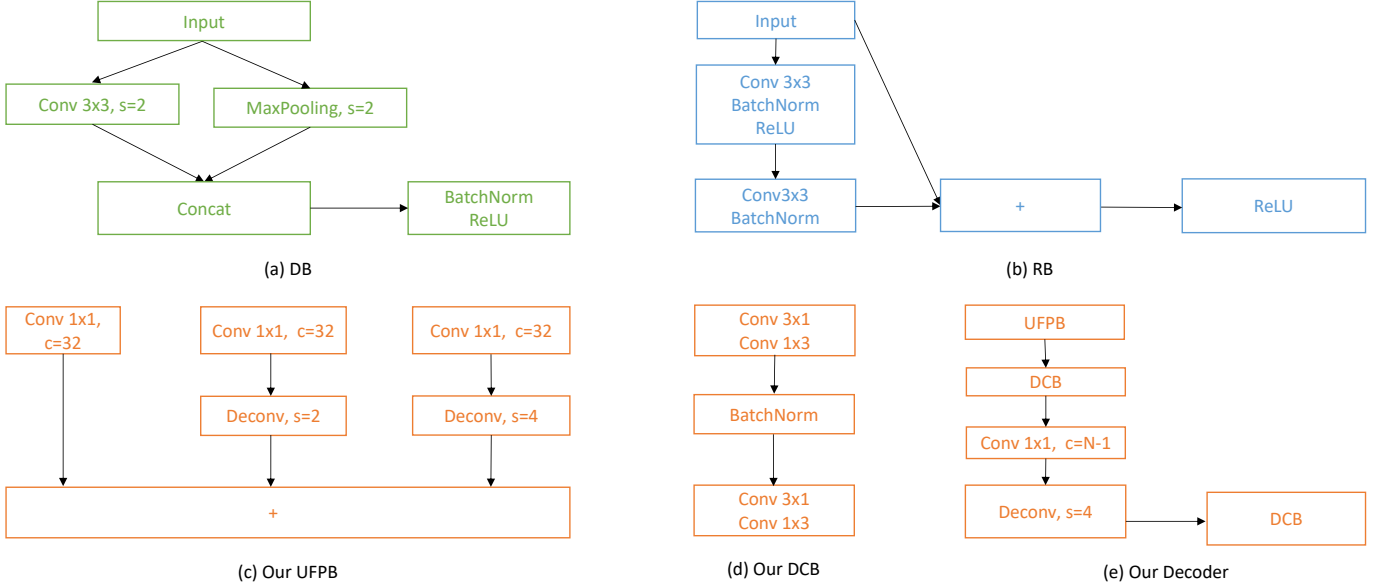


Fig. 3. Specification of CarNet. Here, Conv 3x3 represents the convolution whose kernel size is 3×3 , $s=2$ refers that the stride is 2, and Concat indicates that channel concatenation of feature maps. In addition, BatchNorm refers to batch normalization, ReLU corresponds to Rectified Linear Unit, and Deconv represents transposed convolution. UFPB refers to the up-sampling feature pyramid block, and DCB represents the decomposition convolution block. Besides, $c=32$ means that the output channel of feature maps is 32. N represents the number of categories. For example, N is 2 for crack detection.

In the following, we determine the number of convolutional layers in the intermediate stages. For easy comparison with ResNet34, we let our encoder also have 34 layers. Considering that the four down-sampling blocks and the tail network stage occupy four and four convolutional layers respectively, our encoder could employ seven and six residual blocks in the second and third stages respectively. Note that in ResNet34, besides a convolutional layer in the first stage and a fully connected layer at the end, the remaining stages apply three, four, six, and three residual modules respectively.

Finally, we outline our encoder, as the dotted box is shown in Fig. 2. Through the above design process, one may find that although the number of the total layers is the same, our encoder and ResNet34 differ in the number of the network stages and the number of the convolutional layers in different network stages. Especially, our encoder requires that the number of convolutional layers begins to decrease after the model input is compressed in the initial network stage. As shown in Table I, compared to original ResNet34 as the encoder, our encoder is more efficient and accurate for pixel-wise crack detection.

B. The Proposed Decoder

Here, we introduce our decoder, as shown in Fig. 3 (e):

First, we present a lightweight up-sampling feature pyramid block (UFPB) to capture rich hierarchical features, which is inspired by HED [10] and Deeplab V3+ [16].

Specifically, as shown in Fig. 3 (c), we first use three 1×1 convolutions to compress the last convolutional features in the second, third and fourth stages respectively to make the module lightweight. Note that the compressed channels of feature maps in the three-branch are the same, which are all 32. Then, we do double and quadruple up-sampling on feature maps of the third and fourth stages respectively to make them have the same resolution as those of the second stage. Finally, we fuse convolutional features of different stages with an addition operation.

Next, we construct a decomposition convolution block (DCB) to further enhance the representation of the decoder. Since cracks are mostly linear structures, we employ two cascaded decomposition convolutions (i.e., one 3×1 and 1×3 convolutions respectively) to replace one common 3×3 convolution in the decoder, as shown in Fig. 3 (d).

Then, we utilize one 1×1 convolution to compress the feature maps to $N-1$ channels where N represents the number of categories. Afterward, we restore the compressed feature maps to the model input size by quadruple up-sampling¹.

Finally, we adopt again the module DCB to develop rich convolutional features which are then fed to a sigmoid classifier, as shown in Fig. 3 (e).

In summary, the proposed encoder and decoder networks constitute our overall framework, as shown in Fig. 2. Since it looks like a car, we named it CarNet. In addition, unless otherwise specified, we use the cross-entropy loss to train the proposed architecture.

Comparison with other decoders. Regarding the decoder network, although based on HED and Deeplab V3+, our model is different from them in many aspects. In the following, we briefly state the differences among them on the decoder.

(1) Restoring of feature maps. Deeplab V3+ depends on two quadruple up-sampling to restore the output of the encoder network to the model input size gradually. Besides two quadruple up-sampling, our model utilizes an additional double up-sampling to fuse more feature information, as shown in the module UFPB.

Meanwhile, HED employs more up-sampling with different multiples to restore feature maps of every stage directly to the model input size. Thus, HED needs to adopt large deconvolution kernels during resizing low-resolution feature maps to the model input size, considering that the pixels in them need a large receptive field. Meanwhile, our deconvolution kernels are all 3 in the up-sampling process, which cut down many parameters and calculations.

(2) Objects and methods of feature fusion. Our model takes advantage of features from the last three stages while HED utilizes features from all network stages, and Deeplab V3+ employs features from the second and last stages. Moreover, for information fusion, the other two models adopt channel concatenation while our network applies addition operation, which can cut down parameters and calculations under the same conditions.

(3) Further refinement. Different from HED and Deeplab V3+, we use convolutions to do further refinement after restoring feature maps to the model input size. Considering that cracks are mostly linear structures, and to save calculations, we employ two stacked asymmetric convolutional kernels to replace a common square one.

(4) Number of decoders. Our model and Deeplab V3+ make use of a single decoder while HED utilizes six ones corresponding to one fusion output and five side outputs respectively. Thus, HED needs to weigh the loss functions of different outputs, which contributes to difficulty in model training. In addition, more branch structures increase the memory access cost and thus reduce the inference efficiency of the model.

¹Note that we employ deconvolution for up-sampling in this paper. According to (1) and (2), compared with using deconvolution to compress channels and conduct up-sampling concurrently, our method can reduce space complexity and time complexity. In practice, we adopt deconvolution with kernel size 3.

IV. EXPERIMENTS

In this section, we start with crack detection databases and state detailed implementation. Next, we elaborate on the effectiveness of the proposed network by ablative experiments, and then compare the performance of our model and other state-of-the-art systems on different datasets. Finally, we have a detailed discussion on the inference efficiency of different models.

A. Datasets

We evaluate the proposed network on four public databases, namely our Sun520, our Rain365, BJJN260 [1], and Crack360 [2]. Note that images in the first three databases are captured by the same mobile device, HUAWEI Honor 6X. To make crack data diverse, we choose different streets in Beijing.

Sun520 consists of 520 images captured on sunny days. To our knowledge, in the crack databases using pixel-level annotation, it is the largest open-source one at present. In addition, the time for capturing crack images spans the morning, afternoon, and dusk. In other words, the data is rich in image brightness.

Rain365 contains 365 images captured in the daytime after rain. These crack images refer to the three different backgrounds, i.e., completely wet, partially wet and partially dry, or completely dry. Among them, the full wet backgrounds occupy the majority.

BJN260 embraces 260 images under night scenes in Beijing. The streets at the night are complex and changeable about surrounding environments, such as light source and brightness intensity, which contribute to difficulty for crack detection.

To save computing resources, we resize the resolutions of images in the above three databases from 3968×2240 to 480×320 . On Sun520, Rain365, and BJJN260, we randomly select 400, 300, 200 images for training respectively, and the remaining 120, 65, 60 images for testing respectively.

Besides, to verify the effect of our model on relatively continuous cracks, we utilize CrackTree260 [2] and CRKWH100 [2] for training and testing, respectively. The former contains 260 images where each has 800×600 pixels. These images are cropped to 512×512 during training. The latter embraces 100 images, each of which has 512×512 pixels. For convenience, we unify the above two datasets into one database, Crack360.

B. Implementation Details

Experimental environment: All experiments are conducted on an NVIDIA GeForce GTX 1080Ti with AMD 3700X 8-Core Processor (32G Memory, 1T SSD). We implement our network using the publicly available PyTorch².

Data augmentation: For each of the above databases, we use three data augmentation methods, i.e., rotation, flipping, and adding Gaussian noise. Specifically, we rotate the original training images 180 degrees, and then flip the original images and the rotated images horizontally. Besides, we fulfill Gaussian noise with a normal distribution $N(0, 0.01)$ for the

²<https://github.com/pytorch/pytorch>

original images. Finally, the augmented training set is 5 times as large as the original training set.

Construction of baseline model: Based on ResNet34 [5], we construct the encoder of the baseline model in the experiments. Compared with the original one, the trimmed ResNet34 removes the average pooling layer and the fully connected layer to reduce parameters and calculations.

For the decoder of the benchmark model, we first fuse feature maps of the fourth and third stages, then merge feature maps of the third and second stages, and next restore the fused feature maps to the model input size by quadruple up-sampling. Note that we employ addition operations to fuse feature maps, and utilize deconvolution to perform up-sampling. Finally, to fairly compare the performance of decoders between the benchmark model and the proposed network, we apply two stacked 3×3 convolutions before the sigmoid classifier.

Settings of hyper-parameters: Unless otherwise specified, we employ the full images as the model input. The Adam optimizer [39] is adopted to update network parameters with a mini-batch size of 2 in every iteration. The initial learning rate is set to 3×10^{-4} . We train CarNet with 10,000, 11250, 12,500, and 19,500 iterations on Sun520, Rain365, BJJN260, and Crack360 respectively, which correspond to 10, 15, 25, and 30 epochs respectively. Besides, we set the random seed to a fixed value of 7, to reduce random errors in the experiments.

Evaluation criteria: For test accuracy, we use F_1 score defined as

$$F_1 = \frac{2\mathbf{P}\mathbf{R}}{\mathbf{P} + \mathbf{R}}, \quad \mathbf{P} = \frac{TP}{TP + FP}, \quad \mathbf{R} = \frac{TP}{TP + FN}. \quad (3)$$

Here, \mathbf{P} and \mathbf{R} represent precision and recall, respectively. Besides, TP , FP , and FN refer to true positive, false positive, and false negative, respectively.

When we evaluate the similarity between the prediction image and the ground-truth, it refers to two different threshold methods, i.e., optimal dataset scale (ODS) and optimal image scale (OIS), where the optimal threshold is based on the whole test set and every single test image respectively. In our experiments, we report two F_1 scores by ODS and OIS respectively.

In addition, we present space complexity and time complexity by parameters ($\#\text{para}$) and gigabit floating-point operations per second (GFLOPS). The inference speed is reflected by the average frames per second (FPS) during testing.

C. Ablation Study

In this section, we conduct the ablation experiments on Sun520. The relevant results are shown in Table I. Note that Baseline † and Baseline ‡ correspond to the benchmark model mentioned in IV-B. Their difference is that the output channels in the encoder are the combinations [16, 64, 128, 256] and [64, 128, 256, 512], respectively. In other words, the latter applies the same output channels with the original ResNet34 while the former uses the same output channels with our CarNet. For fair comparisons, other encoders in Table I also employ the same output channels with our encoder.

For convenience, we use the abbreviations shown in the third column of Table I. Specifically, the letters E and D correspond to the encoder and decoder respectively, C and B indicate CarNet and Baseline † respectively, and d represents using the proposed decomposition convolution block to replace two common 3×3 convolutions. Furthermore, $E_C_D_B$ refers to the encoder and decoder networks originated from CarNet and Baseline † , respectively.

TABLE I
ABLATION EXPERIMENTS ON SUN520.

Methods	ODS	OIS	$\#\text{para}$	GFLOPS	FPS
Baseline †	0.4311	0.4437	6.54 M	3.26	108.18
Baseline ‡	0.4441	0.4562	24.9 M	15.59	96.28
$E_C_D_B$	0.4553	0.4674	5.59 M	13.85	101.11
$E_C_D_cB_d$	0.4450	0.4541	4.91 M	11.22	101.41
CarNet	0.5139	0.5158	4.89 M	11.26	104.37

Compared with Baseline † , $E_C_D_B$ improves the test accuracy ODS and OIS by 2.42% and 2.37% respectively while saving 0.95 M parameters. Although in comparison with Baseline † , $E_C_D_B$ increases about 10.6 gigabit floating-point calculations per second, but its test speed only drops by 7 frames per second. It indicates that the proposed encoder achieves a good tradeoff between test accuracy and inference speed. Compared with Baseline ‡ , $E_C_D_B$ yields 1.12% and 1.12% improvements about ODS and OIS respectively, and save 19.31 M parameters and 1.74 GFLOPS calculations, while being about 5 frames per second faster about inference speed. To sum up, compared with enlarging the channels of feature maps, our proposed olive-type encoder is more lightweight, more efficient, and more effective.

Compared with $E_C_D_B$, our CarNet gains advantages in test accuracy, inference speed, and model complexity. Specifically, in comparison with $E_C_D_B$, our CarNet improves 5.86% and 4.84% about ODS and OIS respectively and gains 3.26 frames improvement per second about inference speed, while saving 0.7 M parameters and 2.59 GFLOPS calculations. As these two models apply the same encoder, the above results demonstrate the effectiveness of the proposed decoder.

Note that different from $E_C_D_B$ which utilizes deconvolution to adjust the channels and sizes of feature maps at the current stage to match ones of the previous stage, $E_C_D_cB_d$ first compresses feature maps to 32 channels by 1×1 convolutions, and then resizes the resolutions by double up-sampling. Compared with $E_C_D_cB_d$, the model $E_C_D_B$ gains higher test accuracy. This indirectly shows that the difference in test accuracy between $E_C_D_B$ and our CarNet is not due to the high model complexity of the former, but because our proposed decoder is more reasonable for pixel-wise crack detection.

Meanwhile, by comparing the performance of CarNet and $E_C_D_cB_d$, one may find that the proposed up-sampling feature pyramid block (UFPB) plays an important role in our decoder. Note that CarNet employs quadruple and double up-sampling to resize the resolutions of feature maps from the fourth and third stages respectively while $E_C_D_cB_d$ applies double up-sampling to gradually increase the resolutions. According to Table I, CarNet gains at least 6% improvements

in test accuracy while these two models are almost equivalent in model complexity and inference speed.

D. Performance Comparison on Sun520

TABLE II

THE PERFORMANCE COMPARISON OF DIFFERENT MODELS ON SUN520.

Methods	ODS	OIS	# para	GFLOPS	FPS
RSF [27]	0.4172	0.4660	-	-	-
HED [10]	0.4369	0.4499	14.72 M	47.32	54.10
RCF [11]	0.4397	0.4538	14.8 M	60.16	39.63
BDCN [12]	0.4526	0.4683	16.3 M	84.23	23.97
BDP-Net [13]	0.4877	0.5006	14.8 M	60.16	37.06
FCN8s [14]	0.4352	0.4431	134.27 M	129.53	22.45
U-Net [30]	0.4461	0.4506	31.03 M	128.18	36.46
SegNet [15]	0.4291	0.4334	29.44 M	93.99	40.48
Deeplab V3+ [16]	0.3869	0.4172	40.35 M	59.76	30.19
DeepCrack [2]	0.4402	0.4538	29.48 M	99.85	30.70
CrackSeg [33]	0.4204	0.4259	53.87 M	116.67	16.93
U-CliqueNet [31]	0.4552	0.4686	487.77 K	38.52	27.80
ENet [18]	0.4275	0.4399	349.07 K	1.23	62.20
ERFNet [19]	0.4303	0.4407	2.06 M	8.63	88.07
BiSeNet V1 [34]	0.3941	0.4190	13.25 M	8.74	105.98
FastSCNN [36]	0.3752	0.3853	1.14 M	0.51	110.80
BiSeNet V2 [35]	0.4300	0.4348	3.4 M	7.36	100.19
CarNet	0.5139	0.5158	4.89 M	11.26	104.37

Table II shows the performance of different models on Sun520. Note that we utilize Deeplab V3+ [16] and CrackSeg [33] based on ResNet50. For convenience, according to the numerical value from high to low, we use red, green, and blue colors, to emphasize the experimental results of the top three in test accuracy and inference speed respectively. According to Table II, one may find that:

(1) The proposed CarNet achieves the highest test accuracy on Sun520. First, compared with random structured forests [27], a non-deep learning method, our CarNet achieves nearly 9.67% and 4.98% improvements in ODS and OIS respectively. Second, for ODS and OIS, our CarNet is respectively 2.62% and 1.52% higher than the second-ranked method BDP-Net [13], and respectively 5.87% and 4.72% higher than the third-ranked system U-CliqueNet [31]. In addition, in terms of inference speed, our CarNet is nearly 3 and 4 times as fast as BDP-Net and U-CliqueNet respectively.

(2) The proposed CarNet ranks third in inference speed on Sun520. Although FastSCNN [36] has the fastest inference speed, it does so at the cost of test accuracy. Specifically, our CarNet is 13.87% and 13.05% higher than FastSCNN about ODS and OIS respectively while being only about 6.4 frames per second slower than FastSCNN in terms of inference speed. Meanwhile, CarNet gains 11.98% and 9.68% higher in ODS and OIS respectively than the second fastest model BiSeNetV1 [34] while both models gain almost the same inference efficiency.

In summary, the proposed CarNet gains a good trade-off between test accuracy and inference efficiency. Besides, we display the precision-recall curves of different models on Sun520, as shown in Fig. 4. Compared with other models, our method has significant advantages in the metrics precision, recall, and F_1 score.

Apart from the above quantitative comparison, we also show the qualitative results of different models on Sun520. Considering the length of the article, we mainly show the top

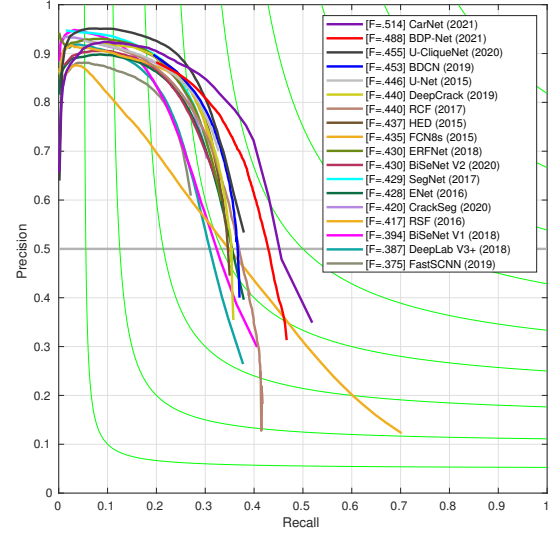


Fig. 4. Precision-Recall curves of different models on Sun520. Note that the metrics precision, recall, and F_1 score, are obtained by using the optimal dataset scale during evaluation.

three systems in terms of inference speed or test accuracy. According to Table II, CarNet has the highest test accuracy and the third-fastest test speed on Sun520, and then we display the prediction results of five approaches based on deep learning. Besides, we also show the related results of random structured forests in Fig. 5.

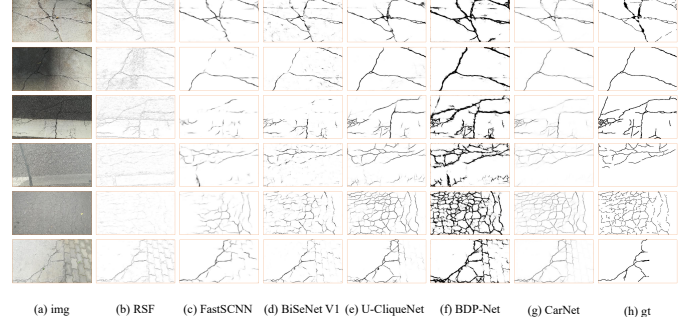


Fig. 5. Qualitative comparison of different models on Sun520. (a) and (h) contain the raw images and the ground-truth, respectively; (b~g) show the images obtained by the corresponding models, respectively. Note that the predicted results are not post-processed in this paper.

Compared with deep learning-based approaches, including our CarNet, random structured forests easily obtain false cracks. Compared with the proposed CarNet, the fast segmentation systems FastSCNN and BiSeNet V1 miss some true cracks while the edge detection method BDP-Net reports some false cracks. The model U-CliqueNet easily gains some false cracks and loses some true cracks, such as the examples in the fourth and fifth lines. We argue that the above phenomena are closely related to the designs of models.

Specifically, as a shallow model, random structured forests can only obtain low-level features and be vulnerable to noise in the background. To develop inference speed, FastSCNN

and BiSeNet V1 employ three consecutive down-sampling with stride 2 in the initial network stage. Accordingly, they recover the feature maps to the model input size by employing eight times up-sampling in the decoders. Although this way improves inference speed, it also easily loses the spatial information in the feature maps, especially when there are trivial cracks in the original input images. At every network stage, BDP-Net fuses the contextual information of feature maps by down-sampling and up-sampling pyramid branch networks respectively. Excessive information fusion easily leads to false cracks. U-CliqueNet modifies U-Net by applying alternately updated modules and two times down-sampling. Because of only owning three network stages, U-CliqueNet focuses on low- and middle-level features, and lacks high-level semantic information, thus easily reporting false small cracks and losing fragments of large cracks.

E. Performance Comparison on Other Databases

To further compare the performance of different models, we conduct the extensive experiments on Rain365, BJD260, and Crack360, respectively.

Specifically, on Rain365, we show the quantitative results in Table III. Compared with BDP-Net and RCF, our CarNet achieves about 3% and 5% gains in ODS, and about 1% and 4% improvement in OIS, respectively. Meanwhile, for inference speed, our model is more than 2 times faster than the above two methods. Compared with FastSCNN and BiSeNet V1, despite a slight drop in inference speed, CarNet attains about 13% and 9% gains in ODS, and nearly 13% and 8% improvement in OIS, respectively.

TABLE III
THE PERFORMANCE COMPARISON OF DIFFERENT MODELS ON RAIN365.

Methods	ODS	OIS	# para	GFLOPS	FPS
RSF [27]	0.4898	0.5277	-	-	-
HED [10]	0.4953	0.5026	14.72 M	47.32	49.50
RCF [11]	0.5071	0.5170	14.8 M	60.16	37.58
BDCN [12]	0.5060	0.5148	16.3 M	84.23	23.16
BDP-Net [13]	0.5305	0.5485	14.8 M	60.16	35.29
FCN8s [14]	0.4999	0.5065	134.27 M	129.53	21.86
U-Net [30]	0.5056	0.5119	31.03 M	128.18	34.57
SegNet [15]	0.4970	0.5051	29.44 M	93.99	37.72
Deeplab V3+ [16]	0.4309	0.4561	40.35 M	59.76	28.47
DeepCrack [2]	0.4929	0.5033	29.48 M	99.85	29.54
CrackSeg [33]	0.4767	0.4794	53.87 M	116.67	16.28
U-CliqueNet [31]	0.5034	0.5122	487.77 K	38.52	26.93
ENet [18]	0.4832	0.4918	349.07 K	1.23	57.46
ERFNet [19]	0.4837	0.4918	2.06 M	8.63	74.59
BiSeNet V1 [34]	0.4693	0.4834	13.25 M	8.74	93.67
FastSCNN [36]	0.4249	0.4327	1.14 M	0.51	100.00
BiSeNet V2 [35]	0.4991	0.5045	3.4 M	7.36	85.57
CarNet	0.5586	0.5595	4.89 M	11.26	89.24

In addition, Fig. 6 shows the precision-recall curves of different models on Rain365. Besides the quantitative results, Fig. 7 displays some qualitative examples. Compared with CarNet, FastSCNN and BiSeNet V1 easily miss true cracks while BDP-Net and RCF often obtain false cracks. For specific analysis, please refer to section IV-D.

On BJD260, we reveals the quantitative results in Table IV. Compared with BDP-Net and RCF, our CarNet obtains significant gain in inference speed while achieving about 2% and 5% improvement in ODS, 1% and 4% improvement in

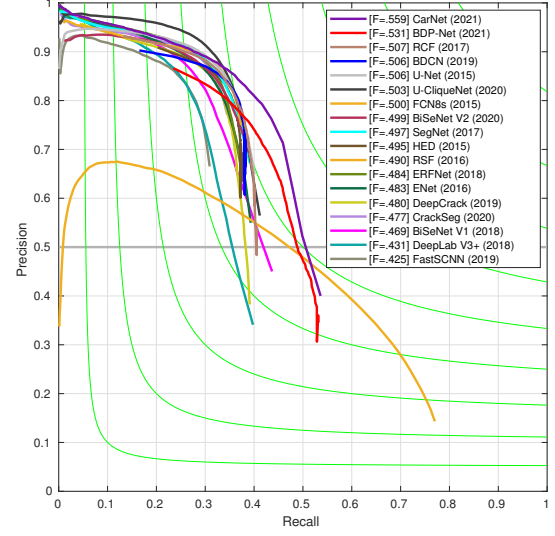


Fig. 6. Precision-Recall curves of different models on Rain365. Here, the metrics precision, recall, and F1 score, are obtained by using the optimal dataset scale during evaluation.

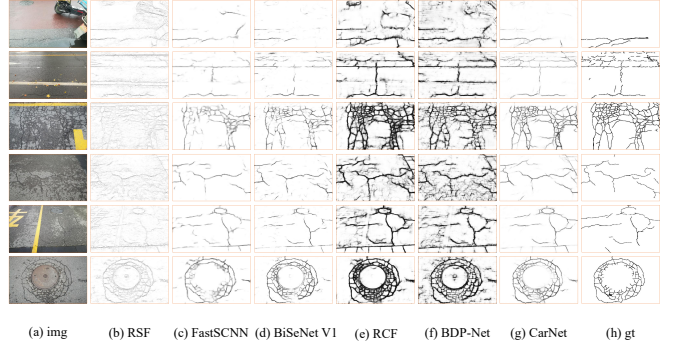


Fig. 7. Qualitative results of different models on Rain365. (a) and (h) contain the raw images and the ground-truth, respectively; (b~g) show the images predicted by the corresponding models, respectively.

TABLE IV
THE PERFORMANCE COMPARISON OF DIFFERENT MODELS ON BJD260.

Methods	ODS	OIS	# para	GFLOPS	FPS
RSF [27]	0.4550	0.4415	-	-	-
HED [10]	0.4943	0.5035	14.72 M	47.32	49.50
RCF [11]	0.5147	0.5228	14.8 M	60.16	37.58
BDCN [12]	0.5203	0.5276	16.3 M	84.23	23.16
BDP-Net [13]	0.5382	0.5414	14.8 M	60.16	35.29
FCN8s [14]	0.5060	0.5101	134.27 M	129.53	21.86
U-Net [30]	0.5123	0.5200	31.03 M	128.18	34.57
SegNet [15]	0.4674	0.4491	29.44 M	93.99	37.72
Deeplab V3+ [16]	0.4225	0.4420	40.35 M	59.76	28.47
DeepCrack [2]	0.4923	0.4955	29.48 M	99.85	29.54
CrackSeg [33]	0.4748	0.4837	53.87 M	116.67	16.28
U-CliqueNet [31]	0.5200	0.5325	487.77 K	38.52	26.93
ENet [18]	0.4852	0.4935	349.07 K	1.23	57.46
ERFNet [19]	0.4787	0.4822	2.06 M	8.63	74.59
BiSeNet V1 [34]	0.4381	0.4583	13.25 M	8.74	93.67
FastSCNN [36]	0.3738	0.3850	1.14 M	0.51	100.00
BiSeNet V2 [35]	0.4872	0.4998	3.4 M	7.36	85.57
CarNet	0.5633	0.5659	4.89 M	11.26	89.24

OIS, respectively. Compared with FastSCNN and BiSeNet V1, despite a slight decrease in inference speed, our CarNet is about 19% and 12% higher in ODS, 18% and 10% higher in OIS, respectively.

Note that BZN260 has a greater difference in the scale of image contents. According to the analysis of the fast segmentation models and general edge detection systems in section IV-D, the larger the multi-scale difference of the image contents, the larger the difference between test accuracy of the fast image segmentation systems and the proposed method, and the smaller the difference between test accuracy of the general edge detection methods and the proposed approach. This conclusion coincides with the quantitative results of different models on BZN260.

Besides, Fig. 8 and Fig. 9 display separately precision-recall curves and predicted examples of different models on BZN260.

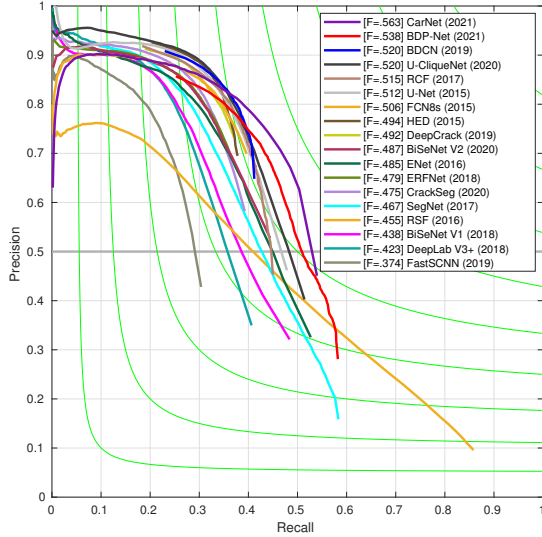


Fig. 8. Precision-Recall curves of different models on BZN260. The above metrics precision, recall, and F_1 score, are obtained by using the optimal dataset scale during evaluation.

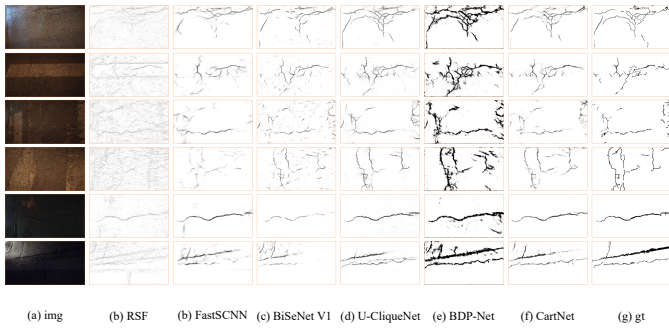


Fig. 9. Qualitative results of different models on BZN260. (a) and (g) contain the raw images and the ground-truth, respectively; (b~f) display the images obtained by the corresponding models, respectively.

On Crack360, according to Table V, compared with ERFNet and ENet, our CarNet gains a slightly higher test accuracy in ODS and OIS while achieving about 20 frames faster per

TABLE V
THE PERFORMANCE COMPARISON OF DIFFERENT MODELS ON CRACK360.

Methods	ODS	OIS	# para	GFLOPS	FPS
RSF [27]	0.6604	0.8148	-	-	-
HED [10]	0.9352	0.9515	14.72 M	81.11	35.32
RCF [11]	0.9311	0.9491	14.8 M	102.67	25.17
BDCN [12]	0.9161	0.9525	16.3 M	143.76	15.05
BDP-Net [13]	0.9214	0.9522	14.8 M	102.67	24.39
FCN8s [14]	0.9440	0.9630	134.27 M	189.5	13.84
U-Net [30]	0.941	0.9529	31.03 M	218.46	22.75
SegNet [15]	0.9407	0.9658	29.44 M	160.11	25.53
DeepCrack [2]	0.9428	0.9694	29.48 M	170.1	19.93
Deeplab V3+ [16]	0.9170	0.9539	40.35 M	101.16	20.25
CrackSeg [33]	0.9434	0.9700	53.87 M	197.47	11.14
U-CliqueNet [31]	0.9364	0.9579	487.77 K	65.57	16.41
ENet [18]	0.9440	0.9589	349.07 K	2.09	53.13
ERFNet [19]	0.9482	0.9714	2.06 M	14.72	58.71
BiSeNet V1 [34]	0.8939	0.9541	13.42 M	15.32	89.73
FastSCNN [36]	0.8790	0.9187	1.14 M	0.87	93.52
BiSeNet V2 [35]	0.9407	0.9699	3.4 M	12.57	80.24
CarNet	0.9536	0.9724	4.89 M	19.31	77.31

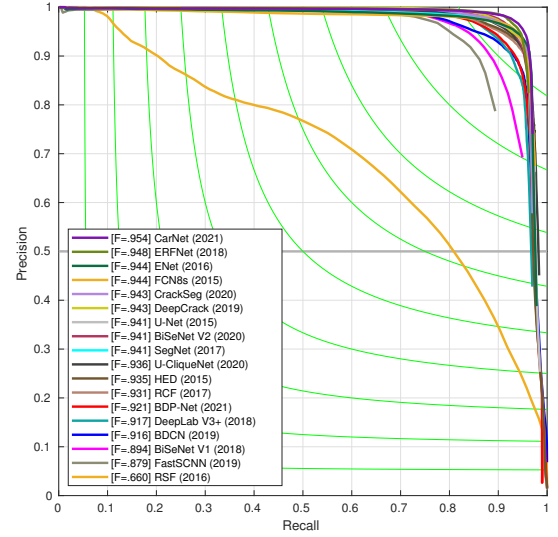


Fig. 10. Precision-Recall curves of different models on Crack360. Note that the above metrics precision, recall, and F_1 score are obtained by using the optimal dataset scale during evaluation.

second in inference speed. Compared with FastSCNN and BiSeNet V1, despite a drop in inference speed, CarNet obtains about 7% and 6% gains in ODS, 5% and 2% improvement in OIS, respectively. Besides, CarNet and BiSeNetV2 [35] have comparable test accuracy and inference speed. In addition, as shown in Fig. 10, we display the precision-recall curves of different models on Crack360.

In terms of test accuracy On Crack360, the fast segmentation models, especially ENet [18], ERFNet [19], and BiSeNetV2 [35], are no less than the general edge detection and image segmentation systems. However, according to Table II, Table III, and Table IV, about test accuracy, these models on Sun520, Rain365, and BZN260 generally does not exceed the general edge detection and image segmentation approaches.

The above phenomenon is mainly due to the distribution of crack data. Specifically, the crack images in Crack360 have few intermittent and trivial cracks, which leads to minor

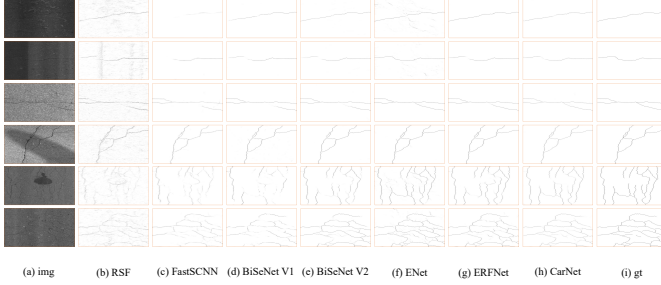


Fig. 11. Qualitative results of different models on Crack360. (a) and (i) contain the raw images and the ground-truth, respectively; (b~h) show the images predicted by the corresponding models, respectively.

differences in the scale of image contents. To easily look at the distribution of crack data and the predicted results of different models, we display some visualization examples in Fig. 11.

F. Discussion on Inference Efficiency

In this section, we discuss the factors that affect inference efficiency. Through section IV-D and IV-E, one can find that inference speed is not uniquely determined by the time complexity of models. For example, on the same database, CarNet can gain faster inference speed than ENet, although our CarNet has about 9 times FLOPS than ENet. In fact, besides time complexity, other factors affect inference speed, such as memory access cost and model parallelism.

ShuffleNet V2 [40] proposed four practical guidelines for efficient networks: (1) Equal input and output channels for a convolution lead to the minimal memory access cost; (2) Too many group convolutions increase memory access cost; (3) The fragmentation of networks usually reduces model parallelism; (4) Element-wise operations cannot be ignored. Below, we use them to analyze why some models fail to infer efficiently.

The edge detection methods HED, RCF, BDCN, and BDP-Net utilize the multi-branch structures, thereby reducing model parallelism. Models, like U-Net, SegNet, and DeepCrack, adopt excessive skip-layer structures which cut down model parallelism. U-CliqueNet frequently employs skip layers in the proposed module. In FCN8s, there are too many element-wise operations in the last three 1×1 convolutional layers. Based on Deeplab V3+, CrackSeg increases new information fusion about low-level features through skip-layer. Although improving test accuracy, this manner also further reduces the parallelism. Deeplab V3+ utilizes enormous bottleneck layers in its encoder, which leads to repeated changes in input and output channels. ENet not only employs the bottleneck layers in its encoder, but also uses the bottleneck layers in its decoder. Although greatly reducing the model complexity, this way also increases memory access cost and then limits ultimate inference efficiency.

Besides the above factors, hardware (such as GPU, CPU, and memory), platform (such as Pytorch, and TensorFlow), and accelerator of GPU also affect the inference speed of models. For example, ERFNet applies asymmetric convolutions to completely replace common 3×3 convolutions in its

architecture. However, CUDA and Cudnn are usually designed to accelerate 3×3 convolutions. Thus, ERFNet is not so efficient in model inference.

V. CONCLUSIONS

In this paper, we introduce the olive-type distribution about the number of the convolutional layers at different network stages in the encoder to weigh test accuracy and inference efficiency. Besides, we propose a lightweight up-sampling feature pyramid block (UFPB) in our decoder to fuse the hierarchical features of the last three stages of the encoder. Then, the proposed encoder and decoder constitute our overall architecture CarNet.

Extensive experiments on four public databases show that: (1) Compared with the general edge detection and image segmentation systems, the proposed method can gain higher test accuracy and inference speed; (2) Compared with efficient image segmentation models for street scenes, despite a slight drop in inference speed, the proposed approach gains significant improvements in test accuracy. To further improve inference efficiency while retaining test accuracy, some methods based on model compression, such as channel pruning [41]–[43], may be helpful.

ACKNOWLEDGMENT

The authors would like to thank all the editors and anonymous reviewers for their careful reading and insightful remarks.

REFERENCES

- [1] K. Li, B. Wang, Y. Tian, and Z. Qi, “Fast and Accurate Road Crack Detection Based on Adaptive Cost-Sensitive Loss Function,” *arXiv preprint arXiv:2106.15510*, 2021.
- [2] Q. Zou, Z. Zhang, Q. Li, X. Qi, Q. Wang, and S. Wang, “DeepCrack: Learning Hierarchical Convolutional Features for Crack Detection,” *IEEE Transactions on Image Processing*, vol. 28, no. 3, pp. 1498–1512, 2019.
- [3] A. Krizhevsky, I. Sutskever, and G. E. Hinton, “Imagenet classification with deep convolutional neural networks,” in *Advances in Neural Information Processing Systems*, 2012, pp. 1097–1105.
- [4] K. Simonyan and A. Zisserman, “Very Deep Convolutional Networks for Large-Scale Image Recognition,” in *International Conference on Learning Representations*, 2015.
- [5] K. He, X. Zhang, S. Ren, and J. Sun, “Deep Residual Learning for Image Recognition,” in *IEEE Conference on Computer Vision and Pattern Recognition*, pp. 770–778.
- [6] R. Girshick, J. Donahue, T. Darrell, and J. Malik, “Rich Feature Hierarchies for Accurate Object Detection and Semantic Segmentation,” in *Computer Vision and Pattern Recognition*, 2014.
- [7] R. Girshick, “Fast R-CNN,” in *Proceedings of the IEEE International Conference on Computer Vision*, 2015, pp. 1440–1448.
- [8] S. Ren, K. He, R. Girshick, and J. Sun, “Faster R-CNN: Towards Real-Time Object Detection with Region Proposal Networks,” *IEEE Transactions on Pattern Analysis and Machine Intelligence*, vol. 39, no. 6, pp. 1137–1149, 2017.
- [9] Q. Zhao, T. Sheng, Y. Wang, Z. Tang, Y. Chen, L. Cai, and H. Ling, “M2Det: A Single-Shot Object Detector based on Multi-Level Feature Pyramid Network,” in *The Thirty-Third AAAI Conference on Artificial Intelligence, AAAI*, 2019.
- [10] S. Xie and Z. Tu, “Holistically-Nested Edge Detection,” in *Proceedings of the IEEE International Conference on Computer Vision*, 2015, pp. 1395–1403.
- [11] Y. Liu, M.-M. Cheng, X. Hu, K. Wang, and X. Bai, “Richer Convolutional Features for Edge Detection,” in *IEEE conference on computer vision and pattern recognition (CVPR)*, 2017, pp. 3000–3009.

[12] J. He, S. Zhang, M. Yang, Y. Shan, and T. Huang, "Bi-Directional Cascade Network for Perceptual Edge Detection," in *Proceedings of the IEEE Conference on Computer Vision and Pattern Recognition*, 2019, pp. 3828–3837.

[13] K. Li, Y. Tian, B. Wang, Z. Qi, and Q. Wang, "Bi-Directional Pyramid Network for Edge Detection," *Electronics*, vol. 10, no. 3, 2021.

[14] J. Long, E. Shelhamer, and T. Darrell, "Fully Convolutional Networks for Semantic Segmentation," in *Proceedings of the IEEE conference on computer vision and pattern recognition*, 2015, pp. 3431–3440.

[15] V. Badrinarayanan, A. Kendall, and R. Cipolla, "SegNet: A Deep Convolutional Encoder-Decoder Architecture for Image Segmentation," *IEEE Transactions on Pattern Analysis and Machine Intelligence*, vol. 39, no. 12, pp. 2481–2495, 2017.

[16] L. C. Chen, Y. Zhu, G. Papandreou, F. Schroff, and H. Adam, "Encoder-Decoder with Atrous Separable Convolution for Semantic Image Segmentation," in *Proceedings of the 18th European Conference on Computer Vision*, 2018.

[17] J. Deng, W. Dong, R. Socher, L. J. Li, and F. F. Li, "ImageNet: A Large-Scale Hierarchical Image Database," in *IEEE Computer Society Conference on Computer Vision and Pattern Recognition*, 2009.

[18] A. Paszke, A. Chaurasia, S. Kim, and E. Culurciello, "ENet: A Deep Neural Network Architecture for Real-Time Semantic Segmentation," *arXiv preprint arXiv:1606.02147*, 2016.

[19] E. Romera, J. M. Alvarez, L. M. Bergasa, and R. Arroyo, "ERFNet: Efficient Residual Factorized ConvNet for Real-Time Semantic Segmentation," *IEEE Transactions on Intelligent Transportation Systems*, vol. 19, no. 1, pp. 263–272, 2018.

[20] P. Subirats, J. Dumoulin, V. Legeay, and D. Barba, "Automation of Pavement Surface Crack Detection Using The Continuous Wavelet Transform," in *International Conference on Image Processing*. IEEE, 2006, pp. 3037–3040.

[21] R. Achanta, F. Estrada, P. Wils, and S. Susstrunk, "Salient Region Detection and Segmentation," in *International Conference on Computer Vision Systems*. Springer, 2008, pp. 66–75.

[22] Y. Hu and C.-X. Zhao, "A Novel LBP Based Methods for Pavement Crack Detection," *Journal of Pattern Recognition Research*, vol. 5, no. 1, pp. 140–147, 2010.

[23] V. Kaul, A. Yezzi, and Y. Tsai, "Detecting Curves with Unknown Endpoints and Arbitrary Topology Using Minimal Paths," *IEEE Trans. Pattern Anal. Mach. Intell.*, vol. 34, no. 10, p. 1952, 2012.

[24] R. Amhaz, S. Chambon, J. Idier, and V. Baltazart, "A New Minimal Path Selection Algorithm for Automatic Crack Detection on Pavement Images," in *IEEE International Conference on Image Processing*, 2014, pp. 788–792.

[25] R. Amhaz, S. Chambon, J. Idier, and V. Baltazart, "Automatic Crack Detection on Two-dimensional Pavement Images: An Algorithm based on Minimal Path Selection," *IEEE Transactions on Intelligent Transportation Systems*, vol. 17, no. 10, pp. 2718–2729, 2016.

[26] H. Oliveira and P. L. Correia, "Automatic Road Crack Detection and Characterization," *IEEE Transactions on Intelligent Transportation Systems*, vol. 14, no. 1, pp. 155–168, 2013.

[27] Y. Shi, L. Cui, Z. Qi, F. Meng, and Z. Chen, "Automatic Road Crack Detection Using Random Structured Forests," *IEEE Transactions on Intelligent Transportation Systems*, vol. 17, no. 12, pp. 3434–3445, 2016.

[28] N. Strisciuglio, G. Azzopardi, and N. Petkov, "Detection of Curved Lines with B-COSFIRE Filters: A Case Study on Crack Delineation," in *17th International Conference on Computer Analysis of Images and Patterns*, 2017, pp. 108–120.

[29] N. Strisciuglio, G. Azzopardi, and N. Petkov, "Robust Inhibition-Augmented Operator for Delineation of Curvilinear Structures," *IEEE Transactions on Image Processing*, vol. 28, no. 12, pp. 5852–5866, 2019.

[30] O. Ronneberger, P. Fischer, and T. Brox, "U-Net: Convolutional Networks for Biomedical Image Segmentation," in *International Conference on Medical image computing and computer-assisted intervention*. Springer, 2015, pp. 234–241.

[31] G. Li, B. Ma, S. He, X. Ren, and Q. Liu, "Automatic Tunnel Crack Detection Based on U-Net and a Convolutional Neural Network with Alternately Updated Clique," *Sensors*, vol. 20, no. 3, p. 717, 2020.

[32] Y. Yibo, Z. Zhisheng, S. Tiancheng, and L. Zhouchen, "Convolutional Neural Networks with Alternately Updated Clique," in *IEEE Conference on Computer Vision and Pattern Recognition*, 2018, pp. 2413–2422.

[33] W. Song, G. Jia, H. Zhu, D. Jia, and L. Gao, "Automated Pavement Crack Damage Detection Using Deep Multiscale Convolutional Features," *Journal of Advanced Transportation*, vol. 2020, pp. 1–11, 2020.

[34] C. Yu, J. Wang, C. Peng, C. Gao, G. Yu, and N. Sang, "BiSeNet: Bilateral Segmentation Network for Real-time Semantic Segmentation," in *Proceedings of the European Conference on Computer Vision (ECCV)*, 2018, pp. 325–341.

[35] C. Yu, C. Gao, J. Wang, G. Yu, C. Shen, and N. Sang, "BiSeNet V2: Bilateral Network with Guided Aggregation for Real-time Semantic Segmentation," *arXiv preprint arXiv:2004.02147*, 2020.

[36] R. P. K. Poudel, S. Liwicki, and R. Cipolla, "Fast-SCNN: Fast Semantic Segmentation Network," in *BMVC*, 2019, p. 289.

[37] S. Ioffe and C. Szegedy, "Batch Normalization: Accelerating Deep Network Training by Reducing Internal Covariate Shift," in *Proceedings of The 32nd International Conference on Machine Learning*, vol. 1, 2015, pp. 448–456.

[38] K. He, X. Zhang, S. Ren, and J. Sun, "Delving Deep into Rectifiers: Surpassing Human-Level Performance on ImageNet Classification," in *IEEE International Conference on Computer Vision*, 2015, pp. 1026–1034.

[39] D. P. Kingma and J. L. Ba, "Adam: A Method for Stochastic Optimization," in *International Conference on Learning Representations*, 2015.

[40] N. Ma, X. Zhang, H.-T. Zheng, and J. Sun, "ShuffleNet V2: Practical Guidelines for Efficient CNN Architecture Design," in *Proceedings of the European Conference on Computer Vision (ECCV)*, 2018, pp. 122–138.

[41] Y. He, X. Zhang, and J. Sun, "Channel Pruning for Accelerating Very Deep Neural Networks," in *2017 IEEE International Conference on Computer Vision (ICCV)*, 2017, pp. 1398–1406.

[42] J.-H. Luo, H. Zhang, H.-Y. Zhou, C.-W. Xie, J. Wu, and W. Lin, "ThiNet: Pruning CNN Filters for a Thinner Net," *IEEE Transactions on Pattern Analysis and Machine Intelligence*, vol. 41, no. 10, pp. 2525–2538, 2019.

[43] X. Chen, Y. Wang, Y. Zhang, P. Du, C. Xu, and C. Xu, "Multi-Task Pruning for Semantic Segmentation Networks," *arXiv preprint arXiv:2007.08386*, 2020.

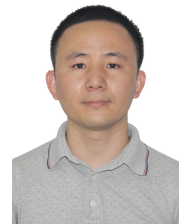
[44] P. Arbeláez, M. Maire, C. Fowlkes, and J. Malik, "Contour Detection and Hierarchical Image Segmentation," *IEEE Transactions on Pattern Analysis and Machine Intelligence*, vol. 33, no. 5, pp. 898–916, 2011.

[45] N. Silberman, D. Hoiem, P. Kohli, and R. Fergus, "Indoor Segmentation and Support Inference from RGBD Images," in *Proceedings of the 12th European Conference on Computer Vision*, 2012.

[46] D. A. Mély, J. Kim, M. McGill, Y. Guo, and T. Serre, "A Systematic Comparison between Visual Cues for Boundary Detection," *Vision Research*, vol. 120, pp. 93–107.

Kai Li is currently working toward the Ph.D. degree with University of Chinese Academy of Sciences, Beijing, China, with a focus on computer vision and machine learning.

His research interests lie in edge detection, image semantic segmentation, and object detection.



Yingjie Tian received the bachelor's degree in mathematics from Shandong Normal University, Jinan, China, in 1994, and the master's degree in applied mathematics from the Beijing Institute of Technology, Beijing, China, in 1997, and the Ph.D. degree in management science and engineering from China Agricultural University, Beijing, China. He is currently a Professor with the Research Center on Fictitious Economy and Data Science, Chinese Academy of Sciences. He has published four books on SVMs.



His research interests include support vector machines, optimization theory and its applications, data mining, intelligent knowledge management, and risk management.



Zhiqian Qi is an associate Professor with the Research Center on Fictitious Economy and Data Science, Chinese Academy of Sciences, Beijing, China.

His research interests include image semantic segmentation, super resolution, object detection, object tracking, change detecting, and statistical machine learning.

APPENDIX

A. The validity of CarNet on Edge Detection

Besides crack detection, we also examine the capability of the proposed CarNet on the edge detection task. To improve the model performance, we also use the pre-trained weights to initialize CarNet. To this end, we first construct a classification network by adding a global pooling layer and a fully connected layer behind our olive-type encoder. Second, we use cross-entropy to train the classification model on ImageNet 1K database³.

In the following, we first introduce edge detection databases and detailed implementation, then compare the performance of our CarNet and other state-of-the-art models.

We conduct experiments on three public datasets, i.e., BSDS500 [44], NYUDv2 [45], and Multicue [46]. BSDS500 contains 200, 100, and 200 images for training, validation, and testing, respectively. NYUDv2 consists of 381, 414, and 654 images for training, validation, and testing, respectively. Multicue contains 80 and 20 images for training and testing, respectively.

In the experiments, for every database, we apply the training and validation datasets (if necessary) for fine-tuning, and the test dataset for evaluation. Regarding data augmentation, we utilize the same strategy as [11]. During training, for BSDS500 and NYUDv2, we employ the full resolution images as the model input. As the original images on Multicue give high resolutions, we adopt the randomly cropped 500×500 image patches as the model input.

The mini-batch size is set to 4, 2, 2 for BSDS500, NYUDv2, and Multicue, respectively. The Adam optimizer [39] is adopted to update network parameters. The learning rate is initially set to 1×10^{-4} , and then divided by 10 after 15 K iterations. The weight decay is set to 2×10^{-4} . We train CarNet with 21 K, 18 K, and 1.5 K iterations on BSDS500, NYUDv2, and Multicue, respectively. Furthermore, we employ non-maximum suppression to produce the thinned edge maps before evaluation.

Through Table VI, Table VII, and Table VIII, we present the test accuracy, space and time complexity, and inference speed of different models on BSDS500, NYUDv2, and Multicue. Note that the test accuracy ODS and OIS are obtained by the single-scale test. Besides, in the above three databases, the sizes of the test images are 321×481 , 425×560 , and 720×1280 , respectively.

³Besides, we employ the hyper-parameter as follow: mini-batch size (128), initial learning rate (1×10^{-2}), momentum (0.9), weight decay (5×10^{-5}), training epochs (60). Regarding the learning rate decay, we use the cosine annealing scheduler.

On BSDS500, our CarNet achieves nearly two times as fast as HED in terms of inference speed while obtaining minor improvements in ODS and OIS respectively. Meanwhile, our model gets two times faster than RCF in inference speed while gaining equivalent test accuracy about ODS and OIS. Compared with BDCN and BDP-Net, despite a slight drop in ODS and OIS, our approach achieves three and two times faster inference speed respectively. Besides, we present the precision-recall curves of different models on BSDS500, as shown in Fig. 12.

TABLE VI

THE PERFORMANCE COMPARISON OF DIFFERENT MODELS ON BSDS500.

Methods	ODS	OIS	# para	GFLOPS	FPS
Human	0.803	0.803	-	-	-
HED [10]	0.788	0.804	14.72 M	48.72	51.47
RCF [11]	0.792	0.809	14.8 M	61.89	37.37
BDCN [12]	0.804	0.82	16.3 M	86.24	23.23
BDP-Net [13]	0.803	0.822	14.81 M	61.92	36.7
CarNet	0.793	0.807	4.89 M	11.66	99.6

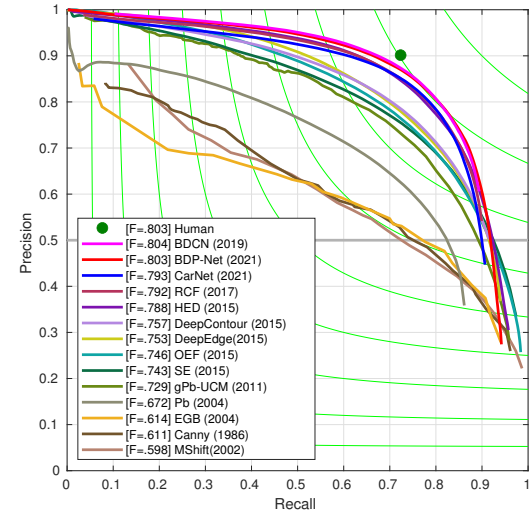


Fig. 12. The precision-recall curves of various approaches using the single-scale test on BSDS500. Note that the metrics precision and recall in this section are obtained by using the optimal dataset scale during evaluation.

On NYUDv2, compared with other systems, our method has a significant advantage in inference speed. Meanwhile, our approach gains comparable test accuracy with BDCN, the state-of-the-art (SOTA) model. In addition, we present the precision-recall curves of different models in Fig. 13(a).

TABLE VII

THE PERFORMANCE COMPARISON OF DIFFERENT MODELS ON NYUDv2.

Methods	ODS	OIS	# para	GFLOPS	FPS
HED [10]	0.741	0.757	14.72 M	73.99	36.35
RCF [11]	0.751	0.77	14.8 M	94.42	28.38
BDCN [12]	0.762	0.776	16.3 M	131.84	16.71
BDP-Net [13]	0.759	0.776	14.81 M	94.46	27.52
CarNet	0.757	0.772	4.89 M	17.6	82.1

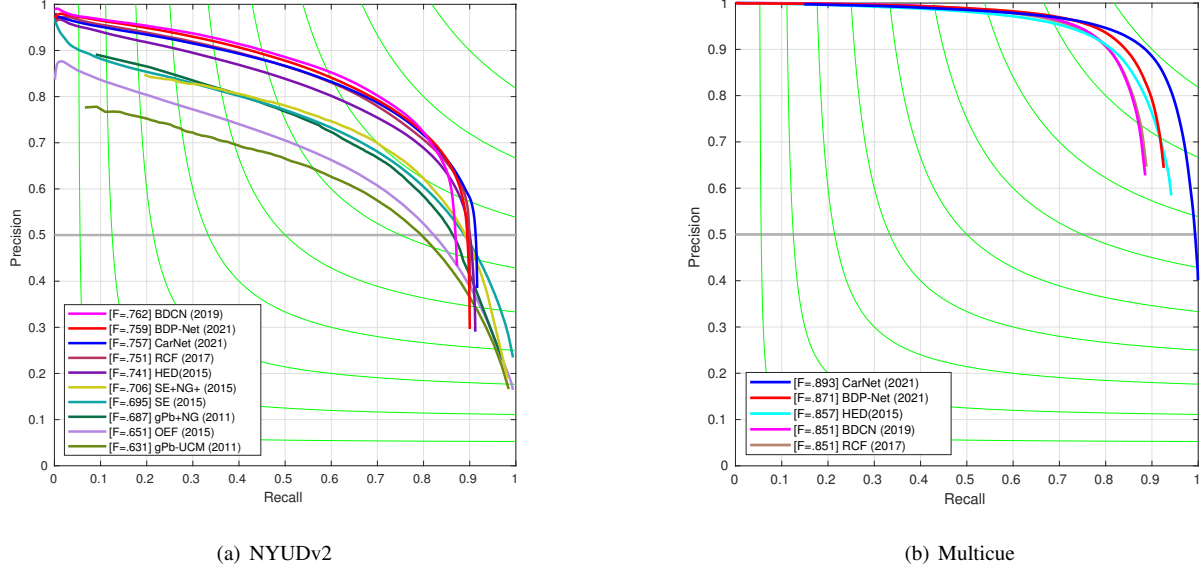


Fig. 13. The precision-recall curves of various approaches using the single-scale test on NYUDv2 and Multicue, respectively.

On Multicue, our CarNet sets new SOTA in test accuracy and inference speed, respectively. In addition, we display the precision-recall curves of different models in Fig. 13(b).

TABLE VIII
THE PERFORMANCE COMPARISON OF DIFFERENT MODELS ON MULTICUE.

Methods	ODS	OIS	# para	GFLOPS	FPS
Human	0.75	-	-	-	-
HED [10]	0.857	0.867	14.72 M	283.9	8.65
RCF [11]	0.851	0.857	14.8 M	363.4	6.68
BDCN [12]	0.851	0.858	16.3 M	507.97	4.03
BDP-Net [13]	0.871	0.877	14.81 M	363.56	6.51
CarNet	0.893	0.9	4.89 M	67.35	18.06

Finally, we also present some visualization examples in Fig. 14. One can find that the differences are relatively small in terms of the prediction results of different models.

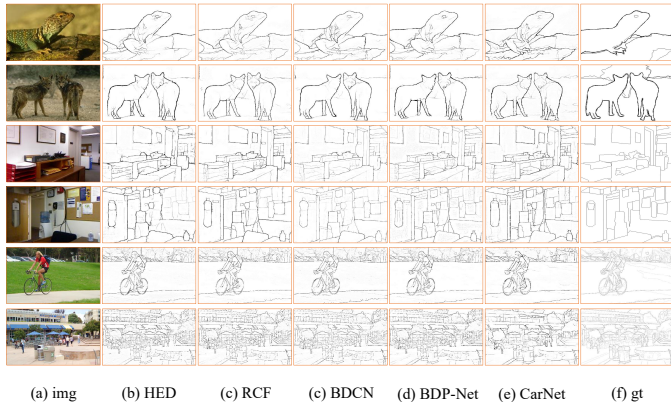


Fig. 14. Visualization examples. (a) and (f) contain the raw images and the ground-truth, respectively. Note that we randomly select two images from each database (BSDS500, NYUD V2, Multicue), and then arrange them in order from top to bottom. (b~e) correspond to the results predicted by these models, respectively.